PHYSICAL REVIEW B **96**, 104413 (2017)

Using rf voltage induced ferromagnetic resonance to study the spin-wave density of states and the Gilbert damping in perpendicularly magnetized disks

Thibaut Devolder[*]
Centre de Nanosciences et de Nanotechnologies, CNRS, Université Paris-Sud, Université Paris-Saclay,
C2N-Orsay, 91405 Orsay cedex, France

(Received 15 March 2017; published 11 September 2017)

We study how the shape of the spin-wave resonance lines in rf voltage induced FMR can be used to extract the spin-wave density of states and the Gilbert damping within the precessing layer in nanoscale magnetic tunnel junctions that possess perpendicular magnetic anisotropy. We work with a field applied along the easy axis to preserve the cylindrical symmetry of the uniaxial perpendicularly magnetized systems. We first describe the experimental setup to study the susceptibility contributions of the spin waves in the field-frequency space. We then identify experimentally the maximum device size above which the spin waves confined in the free layer can no longer be studied in isolation as the linewidths of their discrete responses make them overlap into a continuous density of states. The rf voltage induced signal is the sum of two voltages that have comparable magnitudes: a first voltage that originates from the linear transverse susceptibility and rectification by magnetoresistance and a second voltage that arises from the nonlinear longitudinal susceptibility and the resultant time-averaged change of the exact micromagnetic configuration of the precessing layer. The transverse and longitudinal susceptibility signals have different dc bias dependencies such that they can be separated by measuring how the device rectifies the rf voltage at different dc bias voltages. The transverse and longitudinal susceptibility signals have different line shapes; their joint studies in both fixed field-variable frequency, or fixed frequency-variable field configurations can yield the Gilbert damping of the free layer of the device with a degree of confidence that compares well with standard ferromagnetic resonance. Our method is illustrated on FeCoB-based free layers in which the individual spin waves can be sufficiently resolved only for disk diameters below 200 nm. The resonance line shapes on devices with 90-nm diameters are consistent with a Gilbert damping of 0.011. A single value of the damping factor accounts for the line shape of all the spin waves that can be characterized. This damping of 0.011 exceeds the value of 0.008 measured on the unpatterned films, which indicates that device-level measurements are needed for a correct evaluation of dissipation.

DOI: 10.1103/PhysRevB.96.104413

I. INTRODUCTION

The frequencies of the magnetization eigenmodes of magnetic body reflect the energetics of the magnetization. As a result, the frequency-based methods—the ferromagnetic resonances (FMR) [1] and more generally the spin-wave spectroscopies—are particularly well designed for the metrology of the various magnetic interactions. In particular, measuring the Gilbert damping parameter α that describes the coupling of the magnetization dynamics to the thermal bath, specifically requires high-frequency measurements. There are two main variants of these resonance techniques. The so-called conventional FMR and its modern version, the vector network analyzer [2] (VNA)-FMR, are established techniques to harness the coupling of microwave photons to the magnetization eigenmodes to measure to anisotropy fields [1], demagnetizing fields, exchange stiffness [3], interlayer exchange [4], and spin-pumping [5], most often at film level. More recent methods, like the increasingly popular spin-transfer-torque-(STT)-FMR, are developed [6] to characterize the magnetization dynamics of magnetic bodies embodied in electrical devices possessing a magnetoresistance of some kind.

In conventional FMR or VNA-FMR, the community is well aware that the line shape of a resonance is more complicated than simple arguments based on the Landau-Lifshitz-Gilbert equation would tell. There are, for instance, substantial contributions from microwave shielding effects [7] ("eddy currents") for conductive ferromagnetic films [8] or ferromagnetic films in contact with (or capacitively coupled to) a conductive layers. A hint to this effect is, for instance, to compare the line shapes [8] for the quasiuniform precession mode and the first perpendicular standing spin-wave modes that occur in different resonance conditions. Note that the experimental line shapes are already complex in VNA-FMR despite the fact that the dynamics is induced by simple magnetic fields supposedly well controlled.

In contrast, STT-FMR methods rely on torques (spin-orbit torques (SOT) [9] or STT) that have less hindsight that magnetic fields or that are the targeted measurements. These torques are related to the current across the device and the experimental analysis generally assumes that this current is *in phase* with the applied voltage. This implicitly assumes that the sample is free of capacitive and inductive responses, even at the microwave frequencies used for the measurement. A careful analysis is thus needed when the STT-FMR methods analyze the phase of the device response to separate the contribution of the different torques [6,10,11]. Besides, the quasiuniform mode is often the only one to be analyzed despite the fact that the line shapes of the higher frequency modes can be very different [10]. Finally, an external field is generally applied in a direction that is not a principal direction of the magnetization energy functional [12]. While this maximizes the signal,

---

[*] thibaut.devolder@u-psud.fr

unfortunately, it makes numerical simulation unavoidable to model the experimental responses.

With the progress in MTJ technologies, much larger magnetoresistances are now available [13], such that signals can be measured while maintaining sample symmetries, for instance, with a static field applied collinearly to the magnetization. In addition, high-anisotropy materials can now be incorporated in these MTJs. This leads to *a priori* much more uniform magnetic configurations in which analytical descriptions are more likely to apply. In this paper, we revisit rf voltage induced FMR in a situation where the symmetry is chosen so that all torques should yield *a priori* the same canonical line shape for all spin waves excited in the system. We use PMA MTJ disks of sizes 500 nm, on which a quasicontinuum of more that 20 different spin-wave modes can be detected, down to sizes of 60 nm where only a few discrete spin-wave modes can be detected. We discuss the line shapes of the spin-wave signals with the modest objective of determining if at least the Gilbert damping of the dynamically active magnetic layer can be reliably extracted. We show that the linear transverse susceptibility and the nonlinear longitudinal susceptibilities must both be considered when a finite dc voltage is applied through the device. We propose a methodology and implement it on nanopillars made with a standard MgO/FeCoB/MgO free layer system in which we obtain a Gilbert damping of 0.011 ± 0.0003. This exceeds the value of 0.008 measured on the unpatterned film, which indicates that device-level measurements are needed for a correct evaluation of dissipation.

The paper is organized as follows. The first section lists the experimental considerations, including the main properties of the sample, the measurement setup, and the mathematical post-processing required for an increased sensitivity. The second section discusses the origins of the measured resonance signals and their main properties. The third section describes how the device diameter affects the spin-wave signals in rf voltage induced ferromagnetic resonance. The last section describes how the voltage bias dependence of the spin-wave resonance signals can be manipulated to extract the Gilbert damping of the dynamically active magnetic layer. After the conclusion, an Appendix details the main features of the spectral shapes expected in ideal perpendicularly magnetized systems.

II. EXPERIMENTAL CONSIDERATIONS

A. Magnetic tunnel junctions samples

We implement our characterization technique on the samples described in detail in Ref. [14]. They are tunnel junctions with an FeCoB-based free layer and a hard reference system based on a well compensated [Co/Pt]-based synthetic antiferromagnet. All layers have perpendicular magnetic anisotropy (PMA). The perpendicular anisotropy of the thick ($t = 2$ nm) free layer is ensured by a dual MgO encapsulation and an iron-rich composition. After annealing, the free layer has an areal moment of $M_s t \approx 1.8$ mA and an effective perpendicular anisotropy field $\mu_0(H_k - M_s) = 330\,\text{mT}$. Before pattering, standard ferromagnetic resonance measurements indicated a Gilbert damping parameter of the free layer being $\alpha = 0.008$. Depending on the size of the patterned device, the tunnel magnetoresistance (TMR) is 220% to 250%, for a stack resistance-area product is $\text{RA} = 12\ \Omega\,\mu\text{m}^2$. The devices are circular pillars with diameters varied from 60 to 500 nm. The materials processing and device rf circuitry were optimized for fast switching [14] spin-transfer-torque magnetic random access memories (STT-MRAM [15]); the quasistatic dc switching voltage is ≈600 mV. In the present paper, the applied voltages shall never exceed 100 mV to minimize spin-transfer-torque effects. The fields will always be applied along z, which is the easy magnetization axis. The sample will be maintained in the antiparallel (AP) state.

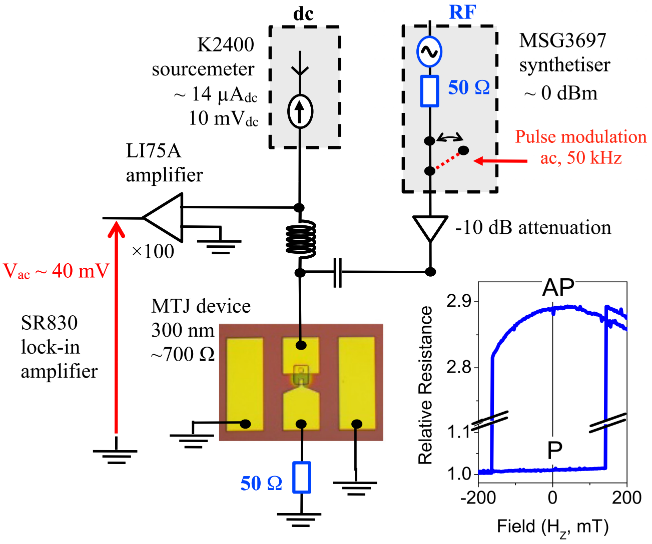

FIG. 1. Sketch of the experimental setup with an $300 \times 300\ \mu\text{m}^2$ optical micrograph of the device circuitry. The given numbers are the typical experimental parameters for a 300-nm diameter junction. (Inset) Resistance vs out-of-plane field hysteresis loop for a device with 300-nm diameter.

B. Measurement setup

The pillars are characterized in a setup (Fig. 1) inspired from spin-torque diode experiments [6] but an electrical bandwidth increased to 70 GHz. The objective is to identify the regions in the {frequency, field} space in which the magnetization is responding in a resonant manner. The device is attacked with an rf voltage V_{rf}. A 10-dB attenuator is inserted at the output port of the synthesizer to improve its impedance matching so as to avoid standing waves in the circuit. This improves the frequency flatness of the amplitude of the stimulus arriving at the device. To ease the detection of the sample's response, the rf voltage is pulse-modulated at an ac frequency $\omega_{\text{ac}}/(2\pi) =$ 50 kHz (Fig. 1). The current passing through the MTJ has thus frequency components at the two sidebands $\omega_{\text{rf}} \pm \omega_{\text{ac}}$. The ac voltage, which appears across the device, is amplified and analyzed by a lock-in amplifier. We shall discuss the origin of this ac voltage in Sec. III. Optionally, the device is biased using a dc sourcemeter supplying V_{dc} and measuring I_{dc}.

Figure 2 shows a representative map of the $\frac{dV_{\text{ac}}}{dH_z}$ response obtained on a pillar of diameter 300 nm with $V_{\text{dc}} = 10$ mV. As positive fields are parallel to the free-layer magnetization, the spin waves of the free layer appear with a positive frequency versus field slope, expected to be the gyromagnetic ratio γ_0 of the free-layer material (see Appendix). Conversely, the

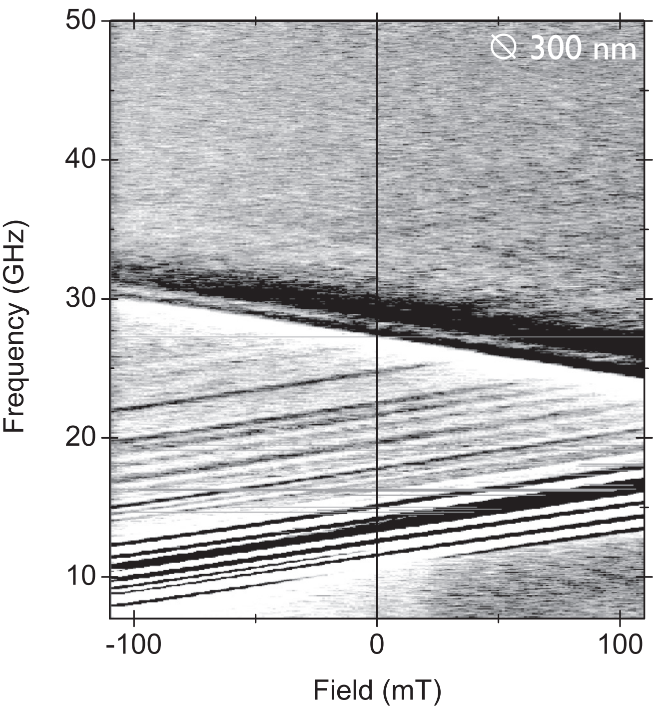

FIG. 2. Field derivative of the rectified voltage $\frac{dV_{\rm ac}}{dH_z}$ in the {frequency-field} parameter space for a 300-nm diameter device in the AP state when the field is parallel to the free layer magnetization. The linear features with positive (respectively, negative) slopes correspond to free layer (resp. reference layers) confined spin-wave modes. Black and white colors correspond to signals exceeding ± 0.01 V/T. The one-pixel high horizontal segments are experimental artifacts due to transient changes of contact resistances.

reference layer eigenmodes appear with a negative slope, expectedly $-\gamma_0$, where this time γ_0 is the gyromagnetic ratio of the reference layer material combination. Working in the AP state is thus a convenient way to easily distinguish between the spin waves of the free layer and of the reference layers. Note that the gyromagnetic ratios γ_0 of the free-layer mode and the reference layer modes differ slightly owing to their difference chemical nature. The free layer has a Landé factor $g = 2.085 \pm 0.015$ where the error bar is given by the precision of the field calibration; the reference layer modes are consistent with a 1.2% larger gyromagnetic ratio. The accuracy of this latter number is limited only by the signal-to-noise ratio in the measurement of the reference layer properties. Looking at Fig. 2, one immediately notices that the linewidths of the reference layer modes are much broader than that of the free layer. While the linewidth of the reference layer modes will not be analyzed here, we mention that this increased linewidth is to be expected for reference layers that contain heavy metals (Pt, Ru) with large spin-orbit couplings, hence larger damping factors [16].

C. Experimental settings

In practice, we choose an applied field interval of [−110,110 mT], which is narrow enough to stay in a state whose resistance is very close to that of the remanent AP state. The frequency $\omega_{\rm rf}/(2\pi)$ is varied from 1 to 70 GHz; we generally could not detect signals above 50 GHz. The practical frequency range $2\pi \times 50\ \text{GHz}/\gamma_0 \approx 1.6$ T is much wider that our accessible field range. For wider views of the experimental signals (for instance when the spin-wave density of states is the studied thing), we shall thus prefer to plot them versus frequency than versus field. The response is recorded pixel by pixel in the {frequency, field} space. The typical pixel size is $\{\delta H_z \times \delta f\} = \{1\ \text{mT} \times 50\ \text{MHz}\}$. The field and frequency resolutions are thus comparable (indeed $2\pi \times \delta f/\gamma_0 = 1.7$ mT).

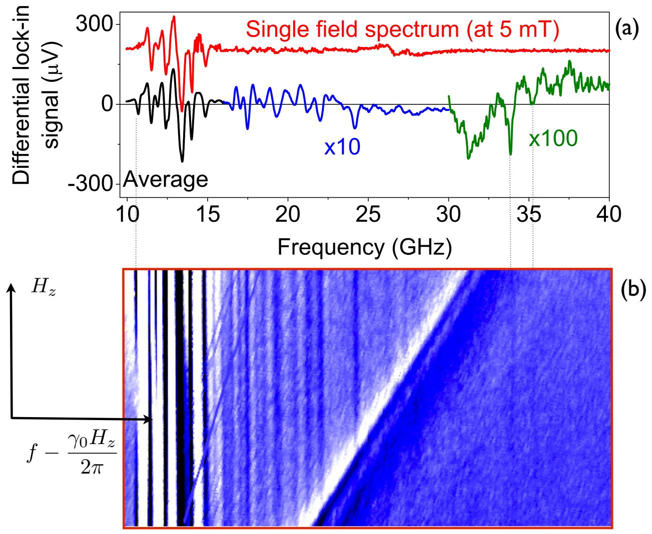

FIG. 3. Illustration of the dynamic range improvement by self-conformal averaging (Sec. II D 2). The procedure is implemented on a 300-nm diameter device to evidence the free-layer modes. (Bottom) Field derivative of the ac signal in the rotated frame in which the modes with $\frac{df}{dH_z} = \frac{\gamma_0}{2\pi}$ should appear as vertical lines. (Top) Comparison of a single field frequency scan (red) with the average over all scans as performed in the $\omega = \gamma_0 H_z$ direction. Note that the signal of the lowest frequency mode (which corresponds to the quasiuniform precession) disappears near zero field, at 5 mT (see the apparent break in the middle of the most left line in the bottom panel).

D. Signal conditioning

1. *Mathematical post-treatments*

Finally, despite all our precautions to suppress the rectifying phenomena that do not originate from magnetization dynamics, we have to artificially suppress the remaining ones. This was done by mathematical differentiation, and we generally plot $\frac{dV_{\rm ac}}{df}$ or $\frac{dV_{\rm ac}}{dH_z}$ in the experimental figures (Figs. 2–5).

2. *Dynamic range improvement by self-conformal averaging*

A special procedure (Fig. 3) is applied when a better signal to noise ratio is desired, while the exact signal line shape and amplitudes are not to meant to be looked at. This procedure harnesses the fact that the normalized shape of the sample's response is essentially self-conformal when moving across a line with $\frac{d\omega}{dH_z} = \gamma_0$ in the {frequency, field} parameter space (see Appendix). The procedure consists in calculating the following primitive:

$$s(f_0) = \frac{1}{2\gamma_0 H_z^{\max}} \int_{\rm contour} \frac{dV_{\rm ac}}{dH_z} df, \tag{1}$$

in which the integration contour is the segment linking the points $(-H_z^{\max}, f_0 - \gamma_0 H_z^{\max})$ and $(H_z^{\max}, f_0 + \gamma_0 H_z^{\max})$ in the {field, frequency} parameter space. Such contours appear as pixel columns in Fig. 3(b). This primitive [Eq. (1)] is efficient to reveal the free-layer spin-wave modes that yield an otherwise too small signal. For instance, when only seven modes can be detected in single field spectra [Fig. 3(a)], the averaging procedure can increase this number to typically above 25. The averaging procedure is also effective in suppressing the signals of the reference layer as these layers average out over a contour designed for the free-layer mode when in the AP state. However, as the linewidth of the free-layer modes is proportional to the frequency, it is not constant across the contour; the higher signal to noise ratio is thus unfortunately obtained at the expense of a distorted (and unphysical) line shape. Note also that this procedure can not be applied to the quasiuniform precession mode as will be explained in Sec. III D 2.

III. ORIGIN AND NATURE OF THE RECTIFIED SIGNAL

Let us now discuss the origin of the demodulated ac voltage. In this section, we assume that the reference layer magnetization is static but not necessarily uniformly magnetized. We can thus express any change of the resistance by writing $\delta R = \frac{\delta R}{\delta M}\delta M$, where δ has to be understood as a functional derivative with respect to the free-layer magnetization distribution.

A. The two origins of the rectified signals

The ac signal can contain two components $V_{1,\mathrm{ac}}$ and $V_{2,\mathrm{ac}}$ of different physical origins [17]. The first component is the "standard" STT-FMR signal: the pulse-modulated rf current is at the frequency sidebands $\omega_{\mathrm{rf}} \pm \omega_{\mathrm{ac}}$ and it rectifies to ac any oscillation of the resistance δR_{rf} occurring at the frequency ω_{rf}. We simply have $V_{1,\mathrm{ac}} = \delta R_{\mathrm{rf}} \times i_{\omega_{\mathrm{rf}} \pm \omega_{\mathrm{ac}}}$.

The second ac signal ($V_{2,\mathrm{ac}}$) is related to the change of the time-averaged resistance due to the population of spin waves created when the rf current is applied [12]. Indeed, the time-averaged magnetization distribution is not the same when the rf is *on* or *off*. This change of resistance δR_{ac} can be revealed by the (optional) dc current I_{dc} passing through the sample, i.e., $V_{2,\mathrm{ac}} = \delta R_{\mathrm{ac}} \times I_{\mathrm{dc}}$.

Note that a third rectification channel [18] can be obtained by a combination of spin pumping and inverse spin Hall effect in in-plane magnetized systems [19]. This third rectification channel yields symmetric Lorentzian lines when applied to PMA systems in out-of-plane applied fields (see Eq. (23) in Ref. [18]) . Besides, the spin pumping is known to be largely suppressed by the MgO tunnel barrier [20], such that we will consider that we can neglect this third rectification channel from now on. In summary, we have

$$V_{1,\mathrm{ac}} = \frac{V_{\mathrm{rf}}}{R+50}\frac{\delta R}{\delta M}\delta M_{\mathrm{rf}} \quad \text{and} \tag{2}$$

$$V_{2,\mathrm{ac}} = \frac{V_{\mathrm{dc}}}{R+50}\frac{\delta R}{\delta M}\delta M_{\mathrm{ac}}. \tag{3}$$

This has important consequences.

B. Compared signal amplitudes in the P and AP states

The first important consequence of Eqs. (2) and (3) is that the signal amplitude depends on the nature of the micromagnetic configuration. As intuitive, both $V_{1,\mathrm{ac}}$ and $V_{2,\mathrm{ac}}$ scale with how much the instantaneous device resistance depends on its instantaneous micromagnetic configuration. This is expressed by the *sensitivity factor* $\frac{\delta R}{\delta M}$, which is essentially a magnetoresistance. We expect no signal when the resistance is insensitive to the magnetization distribution at first order (i.e., when $\frac{\delta R}{\delta M} \equiv 0$).

In our samples, the shape of the hysteresis loop (Fig. 1) seems to indicate that the free layer magnetization is very uniform when in the parallel (P) state. Consistently, the experimental rectified signals were found to be weak when in the P state. Conversely, there is a pronounced curvature in the AP branch of the $R(H_z)$ hysteresis loop (see one example in the inset of Fig. 1). This indicates that the resistance is much dependent on the exact magnetization configuration when in the AP state. Consistently, this larger $\frac{\delta R}{\delta M}$ in the AP state is probably the reason why the rectified signal is much easier to detect in the AP state for our samples.

C. Bias dependence of the rectified signals

The second important consequence of Eqs. (2) and (3) concerns the dependence of the rectified ac signals $V_{1,\mathrm{ac}}$ and $V_{2,\mathrm{ac}}$ on the dc and rf stimuli. As δM_{rf} scales with the applied rf torque according to a linear transverse susceptibility [$\Re e(\chi_{xx})$, see Appendix], $V_{1,\mathrm{ac}}$ is expected to scale with the rf power ${V_{\mathrm{rf}}}^2$ [see Eq. (2)] independently from the dc bias, i.e., we have

$$V_{1,\mathrm{ac}} \propto {V_{\mathrm{rf}}}^2.$$

In contrast, δM_{ac} is related to a longitudinal susceptibility and is thus quadratic with the rf torques (see Appendix). Using Eq. (3), we thus expect the following bias dependence:

$$V_{2,\mathrm{ac}} \propto {V_{\mathrm{rf}}}^2 V_{\mathrm{dc}}.$$

D. Peculiarities of the quasiuniform precession (QUP) mode

The last important consequence of Eqs. (2) and (3) concerns specifically the quasiuniform precession (QUP) mode that shows a peculiar ac signal.

1. *Quasiabsence of STT-FMR like signal for the quasiuniform precession mode*

In the idealized macrospin case (see Appendix), the uniform precession is perfectly circular with no rf variation of M_z at any order. If the fixed layer was uniformly magnetized along exactly z, this would lead to $V_{1,\mathrm{ac}} = 0$ such that the signal of the QUP mode would be given by purely $V_{2,\mathrm{ac}}$. This qualitatively "pure $V_{2,\mathrm{ac}}$ character" is confirmed experimentally by the fact that the signal of the QUP mode systematically changes sign with V_{dc} in our sample series (not shown).

2. *Strong dependence of the QUP signal amplitude with the applied field*

In addition, the experimental signal of the quasiuniform mode is found to disappear at low fields [see Figs. 2, 3(b), 4(a), and 4(b)], exactly at the apex of the AP branch of the

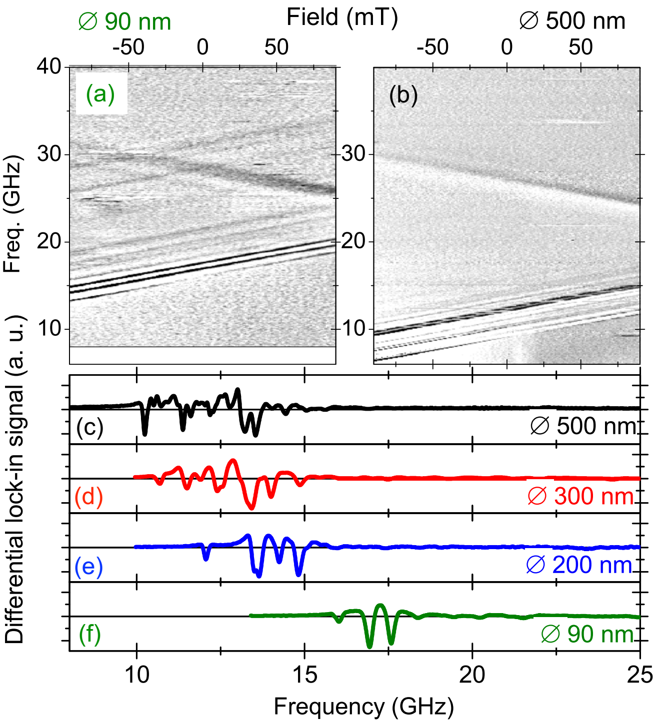

FIG. 4. Dependence of the field derivative of the ac voltage over the device diameter. (Top) Full spectral dependence in the window [6,40GHz] × [−90,90 mT] for 90-nm (left) and 500-nm (right) diameter devices. (Bottom) Frequency dependence of the field derivative of the ac voltage after self-conformal averaging for various device sizes. The signal amplitudes have been normalized to ease their comparison.

hysteresis loop (Fig. 1), i.e., for the field leading specifically to $\frac{dR}{dH_z} = 0$. Moreover, the amplitude of the ac signal of the QUP mode appears to be essentially linearly correlated with the loop slope $\frac{dR}{dH_z}$ (not shown). For instance, the $V_{2,\mathrm{ac}}$ of the QUP mode changes sign when the applied field crosses the apex of the $R(H_z)$ loops (Fig. 1).

The reason stems probably from the sensitivity factor $\frac{\delta R}{\delta M}$ and its correlation with the loop slope $\frac{dR}{dH_z}$; in some sense, a large loop slope should translate in a large sensitivity factor. While a numerical evaluation of this correlation goes beyond the scope of this paper, we stress that if the magnetization was perfectly uniform there would be a one-to-one correlation between loop slope $\frac{dR}{dH_z}$ and magnetoresistance sensitivity factor $\frac{\delta R}{\delta M}$. This trend remains qualitatively true for the QUP mode. Indeed, as the hysteresis loop is monitoring the *spatial average* of the magnetization, it is more insightful for the *uniform mode* than for any other (higher-order) modes whose dynamic profiles spatially average to essentially zero [21]; the correlation between $\frac{dR}{dH_z}$ and $\frac{\delta R}{\delta M}$ is thus expected to be maximal for quasiuniform changes of the magnetization configuration.

While this property—the disappearance of the QUP mode signal when $\frac{dR}{dH_z} = 0$—can be used to distinguish the QUP mode from the higher-order spin waves, the pronounced field dependence of the QUP signal complicates the analysis, as it prevents to conveniently analyze the field derivative of the ac signal (Sec. II D 1). In the remainder of this paper we shall focus on only higher-order modes to avoid such difficulties.

E. Signals for nonuniform spin waves

Before analyzing the spin-wave density of states (Sec. IV), let us comment on the amplitude of the STT-FMR-like signal $V_{1,\mathrm{ac}}$ for the nonuniform spin waves. In the perpendicular magnetization state, these spin waves have a circular precession [22]. By symmetry, the resistance is not expected to change during a period of circular precession when in the perfect collinear cases and for radial spin waves maintaining the cylindrical symmetry of the system. In other words, when the dynamical magnetization of the eigenmode maintains the cylindrical symmetry and when the free and reference layers equilibrium magnetizations follow $\vec{M}_\mathrm{free} \times \vec{M}_\mathrm{ref} = \vec{0}$ everywhere in the (xy) plane, with × being the conventional vector product) the device resistance is not expected to oscillate. While we can not identify to what extent we depart from this ideal situation, we speculate that this perfect collinearity does not happen in practice at least because of finite thermal fluctuations. The effect of thermal fluctuations on the device resistance is not averaged out for nonuniform spin waves, while it could be essentially averaged out for the QUP mode analyzed earlier. In practice a finite variation of the resistance $\delta R_\mathrm{rf} \neq 0$ is always present during a precession period for a nonuniform spin wave. This provides a finite sensitivity to any spin-wave mode. This resistance variation at ω_rf has the spectral shape of a transverse susceptibility term $\Re e(\chi_{xx})$ (see Appendix).

IV. SPIN-WAVE DENSITY OF STATES AGAINST LATERAL CONFINEMENT

Any reliable analysis of a spectral line shape or linewidth requires to determine first how many spin waves contribute to the line shape under study. Therefore, before discussing the line shapes of the individual spin-wave modes, let us determine how the lateral confinement influences the measured rectified signal. The impact of the device diameter on the spectral signals is reported in Fig. 4.

A. Spin waves within the references layers

Figure 4 indicates that the modes of the reference layers have frequencies that are almost not affected by the device diameter. This fact is related to the well compensated character of the synthetic antiferromagnet that composes the reference layers. Indeed, the internal demagnetizing fields compensate to some extent, such that they do not influence the frequency of the acoustical mode of a SAF as much as the anisotropies and the interlayer exchange couplings do.

B. Spin waves within the free layer

Conversely, the frequencies of the modes of the free layer are strongly affected by the device diameter (Fig. 4). First, the modes are pushed to higher frequencies as the device is shrunk. At remanence, the lowest frequency mode is at $f_\mathrm{QUP} =$ 12.3 GHz for a diameter of 500 nm; it reaches 19.5 GHz for 60-nm devices (not shown). Second, the frequency spacing

TABLE I. Summary of the expected line shapes and linewidths for the different signals that can be encountered in rf voltage induced FMR experiments. A hyphen is inserted when the concept is not applicable.

Signal	Spectral shape	Peak-to-peak separation	Full width at half maximum	Zero crossings separation
Expected signals and their stimulus dependence:				
$V_{1,\mathrm{ac}} \propto V_{\mathrm{rf}}^2$	$\Re e(\chi_{xx})$	$2\alpha\omega$	-	-
$V_{2,\mathrm{ac}} \propto V_{\mathrm{rf}}^2 V_{\mathrm{dc}}$	ΔM_z	-	$2\alpha\omega$	-
Signal extraction procedure from experiments:				
$\frac{d}{dH_z} V_{1,\mathrm{ac}}^{exp}$ estimated from $\frac{dV_{\mathrm{ac}}^{exp}}{dH_z}\Big\rvert_{V_{\mathrm{dc}}=0}$	$\frac{d\Re e(\chi_{xx})}{d\omega}$	-	-	$2\alpha\omega$
$\frac{d}{dH_z} V_{2,\mathrm{ac}}^{exp}$ estimated from $\Big[\frac{dV_{\mathrm{ac}}^{exp}}{dH_z}\Big\rvert_{V_{\mathrm{dc}}\neq 0} - \frac{dV_{\mathrm{ac}}^{exp}}{dH_z}\Big\rvert_{V_{\mathrm{dc}}=0}\Big]$	$\frac{d\Im m(\chi_{xx})}{d\omega}$	$\frac{2}{\sqrt{3}}\alpha\omega$	-	-

between the free layer modes increases substantially when downsizing the device.

The first effect—increase of f_{QUP} at downscaling—is indicative of a dependence of some effective fields with the device diameter. Among the effective fields, the only ones that vary with the diameter are the exchange fields (positive contribution to the frequency f_{QUP} if magnetization is nonuniform), the demagnetizing fields (positive contribution to the frequency f_{QUP} at downscaling), and the local effective anisotropy fields in case some process damages alter locally the interface anisotropy at the perimeter of the free layer (negative contribution to the frequency f_{QUP} at downscaling) or alter the local magnetization of the rim of the free layer (positive contribution to the frequency f_{QUP} at downscaling). The exchange fields are related to the nonuniformities of either the static configuration—-the fact that the AP state is not perfectly uniform as inferred previously from the loop in Fig. 1—or nonuniformities of the dynamic magnetization, i.e., the fact that the quasiuniform mode is not a strictly uniform mode. If the frequency increase was due to the sole demagnetizing effects, it could be estimated from the demagnetizing factors of disks [23], which are $N_z \approx 1 - (3\pi/8)t/a$, where t and a are the thickness and radius of the free layer. However, a f_{QUP} against $1/a$ plot (not shown) has a perceivable curvature near all sizes; an unwise linear fit through f_{QUP} against the expected γN_z would give a slope of ≈2.5 T, which is obviously too large for the magnetization of the free layer. This indicates that the sole change of the global shape anisotropy with the device diameter is insufficient to account for the increase of f_{QUP} at downscaling: exchange contributions or nonuniformities induced by process damages also contribute to the frequencies. Exchange contributions should not contribute for the largest devices, however, even for those devices the experimental frequencies are larger than the ones expected from global shape anisotropy only, which argues for some process damages. Since the TMR is almost independent of the device size [14], we can reasonably assume that the MgO/FeCoB interface is not substantially affected by the patterning and that consequently the interface anisotropy is essentially preserved at the rim of the free layer. We conclude that part of the increase of f_{QUP} at downscaling is due to a reduced magnetization (magnetically “dead” or weak zone) near the edges of the free layer. This interpretation is probably very much stack and process technology dependent, hence it should not be considered as general.

The second effect—the increased frequency spacing between the modes at small diameters—is the expected effect of the confinement of the spin waves and the resulting increase of the exchange contribution to the mode frequencies [17]. The eigenmodes of perpendicularly magnetized circular disks are well understood and can be described analytically in a semiquantitative manner [21,24–28]. The frequency spacing between the lowest frequency modes scales with $\gamma_0 H_J$, where $H_J = \frac{2Ak^2}{\mu_0 M_S}$ is a generalized exchange field with A the exchange stiffness. The effective wave vector k is reminiscent of the lateral confinement and reads $k^2 = (u_2^2 - u_1^2)/a^2 \approx 9/a^2$ where u_1 and u_2 are the first zeros of the first and second Bessel functions [21]. The lowest frequency spin-wave modes can be resolved only if their frequency spacing is comparable or greater than their linewidth $2\alpha\gamma_0(H_z + H_k - M_s + H_J)$ (see Appendix).

This condition can be used to define a critical device diameter:

$$a_{\mathrm{crit}}^2 = \frac{9A}{\alpha\mu_0 M_S(H_z + H_k - M_s)}. \tag{4}$$

For large devices with $a \gg a_{\mathrm{crit}}$, we expect to observe a quasicontinuum of overlapping modes above f_{QUP}, while discrete nonoverlapping modes are anticipated in the opposite limit. Typical parameters of an FeCoB-based free layer include a magnetization of $\mu_0 M_s = 1.2$ T and a Gilbert damping of [29] $\alpha = 0.01$. From the quasiuniform mode frequency, we can get our effective anisotropy, which is $H_k - M_s = 330$ kA/m. If the exchange stiffness of the free layer was bulklike (i.e., $A = 22$ pJ/m) like in Ref. [17], the critical diameter would be $2a_{\mathrm{crit}} = 444$ nm. In practice, the small frequency spacings between the modes of our samples indicate that the exchange stiffness of our free layer is in the range of 6–7 pJ/m, i.e., well below the bulk value. This estimate of the exchange stiffness was deduced assuming perfectly pinned boundary conditions for the spin waves at the device edge, which is a questionable [30] assumption. However, the exchange stiffness is anyway weak in the free layer and this can be also qualitatively seen directly from the spin-wave spectroscopy: indeed, the frequency spacing of the lowest modes of the reference layer system is typically twice larger that the frequency spacing of the lowest modes of the free layer [see for instance Fig. 3(b)]. While the reason for this small value of the free layer exchange stiffness is not entirely clear, we emphasize that having such a small exchange stiffness is not uncommon in magnetic systems

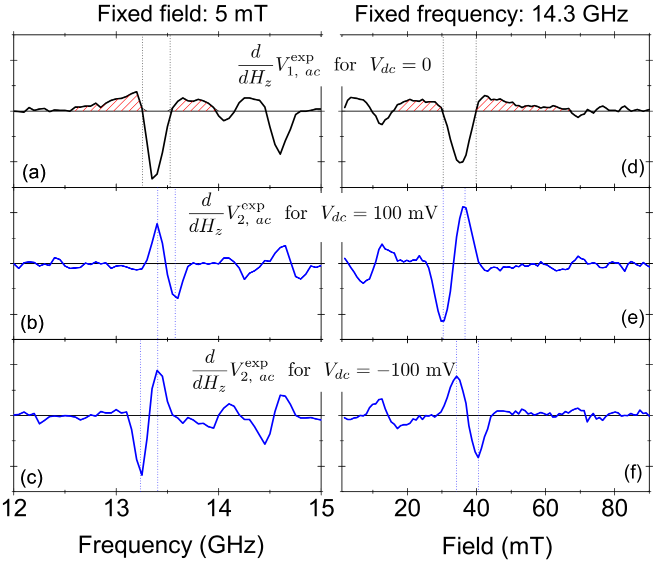

FIG. 5. Rectified ac signals vs frequency at fixed applied field (left) or vs field at fixed frequency (right). The plotted data are $\frac{d}{dH_z}V_{1,\mathrm{ac}}$ [black, (a) and (d)] and $\frac{d}{dH_z}V_{2,\mathrm{ac}}$ [blue, (b), (c), (e), and (f)] as estimated according to the formulas of Table I. The arbitrary vertical scale is the same for all panels. The dotted black lines are separated by 9.5 mT and 270 MHz. The dotted blue lines are separated by 6.1 mT or 170 MHz. These dotted lines correspond to the expected linewidth for a damping of 0.011. (b) is measured for a device different from that of the other panels.

that comprise only a small number of atomic layers, starting, for instance, from 2 pJ/m for a single layer of iron [31]. Anyway, with these parameters, we expect a clear separation of the lowest frequency modes at remanence provided that the device diameter is much smaller than $2a_{\mathrm{crit}} = 250$ nm.

In practice, for 300- and 500-nm devices a fine structure can still be detected in the spin-wave density of states [see Fig. 4(c)] but it is hard to count the modes and guess their frequencies out of this fine structure. In the remainder of this paper, we shall thus only consider devices of diameter less than 200 nm, in which the different spin-wave modes can be unambiguously resolved [see Figs. 4(e) and 4(f)].

V. LINE-SHAPE EVOLUTIONS WITH BIAS AND EXTRACTION OF THE GILBERT DAMPING

Let us now compare the shapes of the experimental rectified signal with those expected (see Appendix). For that purpose we harness the different bias dependencies (Table I) of the rectified signals $V_{1,\mathrm{ac}}$ and $V_{2,\mathrm{ac}}$ to isolate each of them in the experimental signal V_{ac}. We identify $V_{1,\mathrm{ac}}$ to the experimental curve V_{ac} measured at $V_{\mathrm{dc}} = 0$, and we construct an estimate of $V_{2,\mathrm{ac}}$ by subtracting V_{ac} measured at $V_{\mathrm{dc}} = 0$ from that measured at $V_{\mathrm{dc}} \neq 0$ (see Table I). Note because of this subtraction, any dependence of the spin-wave frequency with the dc voltage will prevent the measurement of the voltage dependence of the damping factor or of the voltage dependence of the exciting torques.

We illustrate this procedure in Fig. 5 in which we plot the field derivatives of the so-calculated $V_{1,\mathrm{ac}}$ and $V_{2,\mathrm{ac}}$ rectified signals in both fixed field or fixed frequency experimental conditions for a device of diameter 90 nm. We center the curves on the second lowest frequency eigenmode since it provides the largest signals and it is reasonably separated from both the quasiuniform precession mode and from the other high-order modes. The obtained experimental $V_{1,\mathrm{ac}}$ curves [see Figs. 5(a) and 5(d)] have the expected line shapes (see Appendix) with a negative peak surrounded by two tiny positive halos (areas shaded in red). The separation between the two zero crossings is 9.5 ± 0.5 mT or 285 ± 10 MHz. The obtained experimental $V_{2,\mathrm{ac}}$ curves also have the expected line shape of the derivative of a Lorentzian distribution (see Appendix). As expected, the sign of the response changes with the dc bias voltage. The separation between the positive and negative maxima of the distribution are 6.1 ± 0.5mT and 170 ± 10MHz.

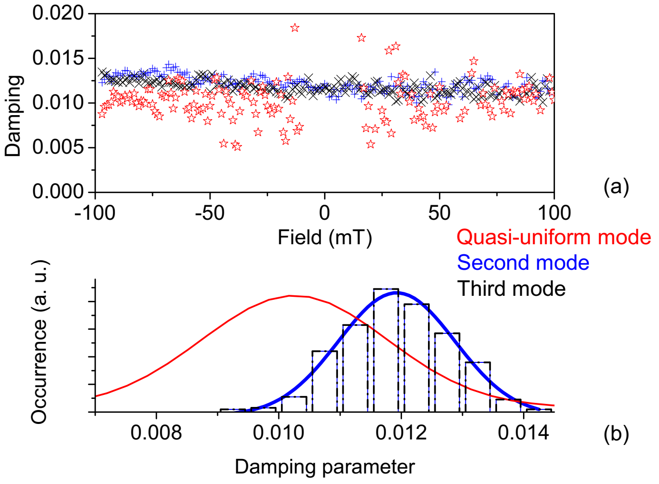

FIG. 6. Statistical view of the Gilbert damping parameters obtained from the fitting of the three lowest spin-wave resonances of a device of 90-nm diameter. For each applied field, the spectral line shapes of the quasiuniform mode are fitted using $\frac{d}{dH_z}V_{2,\mathrm{ac}}$ function (red symbols) while the line shapes of the two next modes are fitted with $\frac{d}{dH_z}V_{1,\mathrm{ac}}$ function (blue and black). (a) gathers the values of the damping parameters that best fit each spectrum recorded at a given applied field. (b) displays the histogram of the distribution of these estimates of the Gilbert damping for the nonuniform modes (dashed-dotted line histogram and its blue Gaussian guide to the eye, of half width 0.0009) and a Gaussian fit (red curve) of the distribution for the quasiuniform mode, of half width 0.0015.

These four different ways of measuring the linewidths [Figs. 5(a), 5(d), 5(b), and 5(e)] are consistent with a free layer damping of $\alpha = 0.011 \pm 0.0003$. Indeed, this value of damping would predict linewidths of $2\alpha f = 295$ MHz and $2\mu_0\alpha\omega/\gamma_0 = 9.54$ mT [materialized as black bars in Figs. 5(a), 5(d) and 5(d)] and $1.15\alpha f = 171$ MHz or $1.15\alpha\omega/\gamma_0 = 6.21$ mT [materialized as blue bars in Figs. 5(b), 5(c), 5(e), and 5(f)].

This proposed value of damping is also consistent with the linewidths of higher-order spin waves that appear at larger frequencies but with a lower signal. This is illustrated in Fig. 6 where a comparison is drawn between the values of the damping estimated for each applied field from the second (and most intense) mode and from the third mode for a device of diameter 80 nm. The used procedure is a direct fit of the experimental line shapes to the derivative of Eq. (A3) with the damping, the resonance frequency, and the signal amplitude as free parameters. For this specific device, the estimates of the damping parameter are subjected to a random error of standard deviation 0.0018 around a mean value of $\alpha = 0.0119$. It is interesting to note that the nonlocal contributions [32,33] to the damping expected for the relatively large wave vectors of the second and third spin-wave modes seem to be too small to be observed in our samples. Note that as mentioned earlier, the same procedure can, in principle, not be applied to the quasiuniform mode since it exhibits a strong dependence of the mode amplitude with the field which invalidates the procedure to some extent. For the sake of completeness of this paper, we have anyway fitted the experimental QUP line shapes with the field derivative of Eq. (A4); this is not possible near zero field, as the corresponding signal vanishes. The value of the Gilbert damping that would be illegitimately deduced would be 0.01, i.e., 20% lower than the correct value. Besides, the estimates from the QUP mode would exhibit a substantially larger spread in the fit results [compare the histograms in Fig. 6(b)]. For these two reasons, we consider that the reliable estimate of the damping is the one extracted from the nonuniform modes.

Above 100 mV of dc bias, the amplitude of the constructed experimental $V_{2,\mathrm{ac}}$ start to depart from proportionality with V_{dc} and a frequency shift is observed, as expected when dc fieldlike spin torques are applied. This comes with by a distortion of the line shape, probably linked to the modification of the spin-wave lifetimes by spin-transfer torque as commonly observed in in-plane magnetized MTJs [34].

VI. SUMMARY AND CONCLUSIONS

In this paper, we have studied how to use rf voltage induced ferromagnetic resonance to study the spin-wave density of states and the Gilbert damping in perpendicularly magnetized disks embodied in magnetic tunnel junctions. We have applied the field along the easy axis to preserve the cylindrical symmetry of the magnetization energy functional. The interest of this configuration is that all the current-induced torques that potentially excite the dynamics yield the same type of susceptibility spectral shape. Additionally, this configuration is the sole in which the applied field and the frequency play similar roles near FMR so that consistency crosschecks between variable-field and variable-frequency experiments can be performed to reveal and suppress potential experimental artifacts.

Working in a situation in which the fixed layer and the free layer are oppositely magnetized is a convenient way to classify the spin waves according to their hosting layer, as the two subsystems have opposite eigenmode frequency-versus-field slopes. The dc bias dependence of the signal of the quasiuniform mode is peculiar and can be used to ambiguously identify the free layer quasiuniform mode in the manifold of spin waves. The nonuniform (higher-order) spin waves are easier to analyze, as their amplitudes weakly depend on the applied field so that field differentiation can be used safely for background subtraction. Optionally, the dynamic range of the experiment can be improved by self-conformal averaging of the resonance spectra.

The unambiguous identification of the spin-wave frequencies requires devices that are sufficiently small to avoid that the spin-wave modes overlap into a quasicontinuous density of states. The critical device size is set by the exchange stiffness, the damping, the magnetization and the effective anisotropy field. In practice, device diameters below 200 nm are needed in our low-damped FeCoB-based PMA system.

For each spin-wave mode, the rf voltage induced spin-wave spectra contain contributions from two different physical mechanisms. The first one is the standard STT-FMR-like signal, whose spectral shape is a linear transverse susceptibility term. It is independent from the dc voltage applied across the MTJ. The second one is a variation of the time-averaged magnetic configuration when the rf voltage is applied. It is proportional to the dc voltage applied across the MTJ and it has the spectral shape of a nonlinear longitudinal susceptibility. The bias dependence can be used to separate these two signals. The analysis of their spectral shape yields the Gilbert damping within the precessing layer. A single value of the damping factor is found to account for the line shapes of all studied spin waves.

The spectra of rf voltage induced rectified voltages for a vanishing dc voltage bias are in principle sufficient to get the Gilbert damping of the dynamically active layer. However, as microwave methods are prone to artifacts, a consistency check exploiting the bias dependence of the resonance spectra is useful for a consolidation of the numerical estimation of the damping.

ACKNOWLEDGMENTS

This work was supported in part by the Samsung Global MRAM Innovation Program, who provided also the samples. Critical discussions with Vladimir Nikitin, Jean-Paul Adam, Joo-Von Kim, and Paul Bouquin are acknowledged.

APPENDIX: SUSCEPTIBILITIES IN AN IDEALIZED PMA FILM

In this Appendix, our aim is to determine the transverse and longitudinal microwave susceptibility versus frequency f and static field H_z for a PMA film as a response to an harmonic transverse field $h_x \cos(\omega t)\vec{e_x}$. We shall write the equations with this transverse field h_x but any other effect that yields a torque possessing a component transverse to the static magnetization will yield similar line shapes. This includes current-induced Oersted-Ampere fields but also Slonczewski STT and fieldlike STT as soon as the reference layer magnetization $\vec{M}_{\mathrm{ref}}$ is not strictly collinear with that of the free-layer $\vec{M}_{\mathrm{free}}$. The susceptibility tensor will be used to deduce the shape of the line expected in rf voltage induced FMR, as summarized in Table I. Throughout this Appendix, we assume a dc field H_z perfectly perpendicular to the plane and a free layer magnetization $\vec{M} = M_z\vec{e}_z + m_x\vec{e}_x + m_y\vec{e}_y$, where the transverse terms are assumed small and written as complex numbers in the frequency space. For convenience, we will use the notation $H' = H_z + H_k - M_s$. We shall also write the frequencies in field units and define $\omega' = \omega/\gamma_0$. This is meant to emphasize the fact that the generalized field H' and the generalized frequency ω' play very similar roles in the FMR of perpendicularly magnetized macrospin when near resonance. We shall systematically assume that $\alpha \ll 1$ and only keep the lowest order of the damping terms in the equations. In

Sec. A 1–A 3, we make the macrospin approximation. This approximation is discussed in Sec. A 4.

1. Transverse linear susceptibility

Following the usual procedure, we project the linearized Landau-Lifshitz-Gilbert equation along $\vec{e}_x$ et $\vec{e}_y$:

$$H'(m_y + \alpha m_x) + i m_x \omega' = h_x M_s \alpha$$

$$H'(m_x - \alpha m_y) - i m_y \omega' = h_x M_s.$$

We then invert this system of equations to get the susceptibilities $m_x = \chi_{xx} h_x$ and $m_y = \chi_{yx} h_x$. They are

$$\chi_{xx} = \frac{M_s H'}{H'^2 - \omega'^2 + 2\mathrm{i}\alpha H'\omega'} \tag{A1}$$

and

$$\chi_{yx} = -\mathrm{i}\frac{M_s \omega'}{H'^2 - \omega'^2 + 2\mathrm{i}\alpha H'\omega'}. \tag{A2}$$

Several points are worth to remind. (i) The dc transverse susceptibilities are $\chi_{xx}^{\mathrm{dc}} = M_s/H'$ and $\chi_{yx}^{\mathrm{dc}} = 0$. (ii) The in-phase transverse susceptibility χ_{xx} is peaked at the FMR condition $\omega' = H'$. It reaches $\chi_{xx}^{\mathrm{FMR}} = -\frac{1}{2i\alpha}\chi_{xx}^{\mathrm{dc}}$. (iii) When near the FMR condition, we have $\chi_{yx} \approx -i\,\chi_{xx}$. Hence the two transverse components of the magnetization are in quadrature and the forced precession is essentially circular. Note that this holds true despite the fact that the pumping field is linearly polarized [i.e., along (x) only]. It would also remain true for other (e.g., STT) pumping torques.

From Eq. (A1) we deduce the classical expressions for the real and imaginary parts of the transverse susceptibility:

$$\Re e(\chi_{xx}) = \frac{M_s H'(H'^2 - \omega'^2)}{4\alpha^2 H'^2\omega'^2 + (H'^2 - \omega'^2)^2}, \tag{A3}$$

$$\Im m(\chi_{xx}) = -\frac{2\alpha M_s \omega' H'^2}{4\alpha^2 H'^2\omega'^2 + (H'^2 - \omega'^2)^2}. \tag{A4}$$

The line shapes given by the above expressions are shown in Fig. 7. Their main properties are summarized in Table I.

2. Longitudinal nonlinear susceptibility

Let us now express the nonlinear change of the longitudinal magnetization ΔM_z that occurs due to the precession. This can be viewed as an rf-induced reduction of the remanence. Using the circularity of the precession near the FMR resonance and the conservation of the magnetization norm to second order in $m_{x,y}$, one gets

$$\Delta M_z \approx \frac{||h_x||^2}{2M_S}\frac{M_s^2 H'^2}{[H'^2 - \omega'^2]^2 + 4\alpha^2 H'^2\omega'^2}, \tag{A5}$$

where $||h_x||$ is the (constant) amplitude of the applied rf field. It is worth noticing that the longitudinal loss of the magnetization is *stationary (constant in time)* despite the fact that the magnetization precesses continuously.

3. Line shapes and linewidths of the susceptibilities and their derivatives

The different susceptibility expressions are plotted in Fig. 7. The line shape of the functions ΔM_z and χ_{xx} are essentially determined by their denominator, which are the fast varying functions of Eqs. (A4) and (A5). As χ_{xx} and ΔM_z are two signatures of the same resonance process, their denominators are equal [see Eqs. (A4) and (A5)] and a simple algebra confirms that $\Im m(\chi_{xx})$ and ΔM_z lead to the same frequency or field linewidths (half width at half maximum), which are

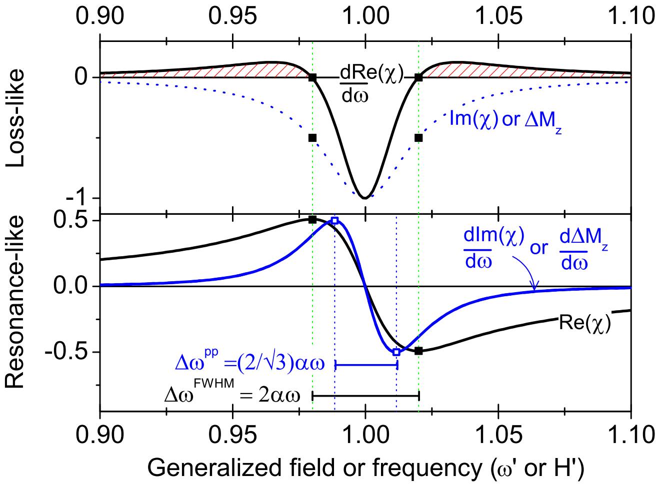

FIG. 7. Transverse susceptibilities, longitudinal susceptibility, and their derivatives in the PMA macrospin model. The curves are plotted for $\alpha = 0.02$ and a resonance condition of unity. The responses amplitudes have been normalized to ease the comparison between the different line shapes. The black horizontal segment in the bottom panel is the FWHM of $\Im m(\chi_{xx})$ and ΔM_z or equivalently the peak-to-peak separation of $\Re e(\chi_{xx})$ (also sketched as the black square dots). The blue segment sketches the peak-to-peak separation of $\frac{d\Im m(\chi_{xx})}{d\omega'}$ (also sketched as the empty blue square dots). The area shaped in red is the positive halo that surrounds the main (negative) peak in $\frac{d\Re e(\chi_{xx})}{d\omega'}$.

$$\Delta\omega = 2\alpha\omega \quad \text{or equivalently,} \quad \Delta H_z = 2\alpha H'. \tag{A6}$$

Note that $\Delta\omega$ (respectively, ΔH_z) is also the frequency (respectively, field) spacing between the positive maximum and negative maximum of $\Re e(\chi_{xx})$ about the FMR condition.

We stress that this linewidth is *different* from that obtained by conventional FMR in which people examine the *derivative* of the absorption signal $\frac{d\Im m(\chi_{xx})}{dH_z}$ versus H_z. The peak-to-peak separation of the conventional FMR signal is $\Delta H_z = \frac{2}{\sqrt{3}}\alpha H' = \frac{2}{\sqrt{3}}\alpha\omega'$. The factor $2/\sqrt{3}$ is 1.1547. The spectral shapes of $\Re e(\chi_{xx})$ and ΔM_z as deduced above are to be used in the main part of the paper to describe, respectively, $V_{1,\mathrm{ac}}$ and $V_{2,\mathrm{ac}}$ (Table I).

4. Linewidth beyond the macrospin approximation

Some words of caution are needed as the calculations done so far the Appendix are for the uniform precession mode of a macrospin, while most of our experimental results were obtained on the higher-order (nonuniform) spin waves. When modeling nonuniform spin waves, one needs to take into account additional exchange and dipole-dipole terms.

For nonuniform spin waves in perpendicularly magnetized system, the exchange fields related to the non uniformity of the dynamical magnetizations m_x and m_y can be added to H'

to form a new generalized field $\tilde{H} = H + H_k - M_s + \frac{2Ak^2}{\mu_0 M_S}$, where k is a generalized wave vector [21,26,28]. The additional exchange contributions act on m_x and m_y on equal footing, hence they maintain the circularity of the precession. The Gilbert linewidth for a nonuniform spin wave is simply [35,36]

$$\Delta\omega = \alpha\omega_k \frac{\partial\omega_k}{\gamma_0 \partial\tilde{H}}, \tag{A7}$$

where this equation holds as $\tilde{H}$ is a circular term. As a result of Eq. (A7), the proportionality of an eigemode linewidth to its frequency [Eq. (A6)] is not broken by the exchange contributions in nonuniform spin waves.

Conversely, the directional nature of the dipole-dipole interaction is such that the related effective fields act differently on the two dynamical magnetizations m_x and m_y for spin waves having a nonradial character. As a result, the dynamic demagnetizing fields can not be simply added to the circular precession H' term and they induce some ellipticity of the precession of the nonuniform spin waves. Dipole-dipole interactions make the eigenmode frequency nonlinear with the field (see Eq. (52) in Ref. [22]). For the lowest lying nonuniform spin wave, the dipole-dipole stiffness field is $M_S kt/2$ with $k \approx \pi/a$. It is negligible against the generalized field $\tilde{H}$ for the thickness used in practice in PMA systems meant for spin-torque applications. The precession stays therefore essentially circular for all the modes observed experimentally here; we will thus consider that it is legitimate to use Eq. (A6) and deduce the damping from the ratio of the half frequency linewidth to the eigenmode frequency.

Finally, we would like to mention that our method is not restricted to the PMA materials only: it should hold when the considered spin waves are quasicircular. In particular, this is the case of exchange-dominated spin waves in in-plane magnetized systems [37].

[1] C. Kittel, Phys. Rev. **73**, 155 (1948).

[2] C. Bilzer, T. Devolder, P. Crozat, C. Chappert, S. Cardoso, and P. P. Freitas, J. Appl. Phys. **101**, 074505 (2007).

[3] T. Kubota, J. Hamrle, Y. Sakuraba, O. Gaier, M. Oogane, A. Sakuma, B. Hillebrands, K. Takanashi, and Y. Ando, J. Appl. Phys. **106**, 113907 (2009).

[4] T. Devolder, J. Appl. Phys. **119**, 153905 (2016).

[5] S. Mizukami, Y. Ando, and T. Miyazaki, J. Magn. Magn. Mater. **226–230**, 1640 (2001).

[6] A. A. Tulapurkar, Y. Suzuki, A. Fukushima, H. Kubota, H. Maehara, K. Tsunekawa, D. D. Djayaprawira, N. Watanabe, and S. Yuasa, Nature (London) **438**, 339 (2005).

[7] M. Bailleul, Appl. Phys. Lett. **103**, 192405 (2013).

[8] Z. Lin and M. Kostylev, J. Appl. Phys. **117**, 053908 (2015).

[9] L. Liu, T. Moriyama, D. C. Ralph, and R. A. Buhrman, Phys. Rev. Lett. **106**, 036601 (2011).

[10] J. C. Sankey, Y.-T. Cui, J. Z. Sun, J. C. Slonczewski, R. A. Buhrman, and D. C. Ralph, Nat. Phys. **4**, 67 (2008).

[11] H. Kubota, A. Fukushima, K. Yakushiji, T. Nagahama, S. Yuasa, K. Ando, H. Maehara, Y. Nagamine, K. Tsunekawa, D. D. Djayaprawira, N. Watanabe, and Y. Suzuki, Nat. Phys. **4**, 37 (2008).

[12] X. Cheng, J. A. Katine, G. E. Rowlands, and I. N. Krivorotov, Appl. Phys. Lett. **103**, 082402 (2013).

[13] S. Ikeda, J. Hayakawa, Y. Ashizawa, Y. M. Lee, K. Miura, H. Hasegawa, M. Tsunoda, F. Matsukura, and H. Ohno, Appl. Phys. Lett. **93**, 082508 (2008).

[14] T. Devolder, A. L. Goff, and V. Nikitin, Phys. Rev. B **93**, 224432 (2016).

[15] A. V. Khvalkovskiy, D. Apalkov, S. Watts, R. Chepulskii, R. S. Beach, A. Ong, X. Tang, A. Driskill-Smith, W. H. Butler, P. B. Visscher, D. Lottis, E. Chen, V. Nikitin, and M. Krounbi, J. Phys. D **46**, 074001 (2013).

[16] V. Kamberský, Phys. Rev. B **76**, 134416 (2007).

[17] T. Devolder, J.-V. Kim, L. Nistor, R. Sousa, B. Rodmacq, and B. Dieny, J. Appl. Phys. **120**, 183902 (2016).

[18] J. N. Kupferschmidt, S. Adam, and P. W. Brouwer, Phys. Rev. B **74**, 134416 (2006).

[19] L. Mihalceanu, S. Keller, J. Greser, D. Karfaridis, K. Symeonidis, G. Vourlias, T. Kehagias, A. Conca, B. Hillebrands, and E. T. Papaioannou, Appl. Phys. Lett. **110**, 252406 (2017).

[20] A. A. Baker, A. I. Figueroa, D. Pingstone, V. K. Lazarov, G. van der Laan, and T. Hesjedal, Sci. Rep. **6**, 35582 (2016).

[21] O. Klein, G. de Loubens, V. V. Naletov, F. Boust, T. Guillet, H. Hurdequint, A. Leksikov, A. N. Slavin, V. S. Tiberkevich, and N. Vukadinovic, Phys. Rev. B **78**, 144410 (2008).

[22] B. A. Kalinikos and A. N. Slavin, J. Phys. C **19**, 7013 (1986).

[23] K. Mizunuma, M. Yamanouchi, H. Sato, S. Ikeda, S. Kanai, F. Matsukura, and H. Ohno, Appl. Phys. Express **6**, 063002 (2013).

[24] G. N. Kakazei, P. E. Wigen, K. Y. Guslienko, V. Novosad, A. N. Slavin, V. O. Golub, N. A. Lesnik, and Y. Otani, Appl. Phys. Lett. **85**, 443 (2004).

[25] R. E. Arias and D. L. Mills, Phys. Rev. B **79**, 144404 (2009).

[26] V. V. Naletov, G. de Loubens, G. Albuquerque, S. Borlenghi, V. Cros, G. Faini, J. Grollier, H. Hurdequint, N. Locatelli, B. Pigeau, A. N. Slavin, V. S. Tiberkevich, C. Ulysse, T. Valet, and O. Klein, Phys. Rev. B **84**, 224423 (2011).

[27] S. V. Nedukh, S. I. Tarapov, D. P. Belozorov, A. A. Kharchenko, V. O. Golub, I. V. Kilimchuk, O. Y. Salyuk, E. V. Tartakovskaya, S. A. Bunyaev, and G. N. Kakazei, J. Appl. Phys. **113**, 17B521 (2013).

[28] K. Munira and P. B. Visscher, J. Appl. Phys. **117**, 17B710 (2015).

[29] T. Devolder, J.-V. Kim, F. Garcia-Sanchez, J. Swerts, W. Kim, S. Couet, G. Kar, and A. Furnemont, Phys. Rev. B **93**, 024420 (2016).

[30] K. Y. Guslienko, S. O. Demokritov, B. Hillebrands, and A. N. Slavin, Phys. Rev. B **66**, 132402 (2002).

[31] N. Romming, A. Kubetzka, C. Hanneken, K. von Bergmann, and R. Wiesendanger, Phys. Rev. Lett. **114**, 177203 (2015).

[32] H. T. Nembach, J. M. Shaw, C. T. Boone, and T. J. Silva, Phys. Rev. Lett. **110**, 117201 (2013).

[33] W. Wang, M. Dvornik, M.-A. Bisotti, D. Chernyshenko, M. Beg, M. Albert, A. Vansteenkiste, B. V. Waeyenberge, A. N. Kuchko,

V. V. Kruglyak, and H. Fangohr, Phys. Rev. B **92**, 054430 (2015).

[34] S. Petit, C. Baraduc, C. Thirion, U. Ebels, Y. Liu, M. Li, P. Wang, and B. Dieny, Phys. Rev. Lett. **98**, 077203 (2007).

[35] A. N. Slavin and P. Kabos, IEEE Trans. Magn. **41**, 1264 (2005).

[36] J.-V. Kim, Phys. Rev. B **73**, 174412 (2006).

[37] M. Dvornik and V. V. Kruglyak, Phys. Rev. B **84**, 140405 (2011).